RSC Advances

PAPER

View Article Online
View Journal | View Issue

Cite this: *RSC Adv.*, 2020, **10**, 15346

IL-6-targeted ultrasmall superparamagnetic iron oxide nanoparticles for optimized MRI detection of atherosclerotic vulnerable plaques in rabbits†

Huaqiang Mo,‡[ab] Chenxing Fu,‡[ab] Zhiye Wu,[ab] Peng Liu,[ab] Zhibo Wen,[c] Qingqing Hong,[ab] Yanbin Cai *[ab] and Gongxin Li*[ab]

Received 14th December 2019
Accepted 4th April 2020

DOI: 10.1039/c9ra10509c

rsc.li/rsc-advances

Vulnerable plaques of atherosclerosis (AS) are the main culprit lesion for the serious risk of acute cardiovascular disease (CVD). Therefore, developing new non-invasive methods to detect vulnerable plaques and to evaluate their stability effectively is of great value in the early diagnosis of CVD. IL-6 plays a vital role in the development and rupture of AS. In this study, IL-6-targeted superparamagnetic iron oxide nanoparticles (Anti-IL-6-USPIO) are synthesized by a chemical condensation reaction. An AS model was established by damaging rabbit abdominal aortic intima with Foley's tube in combination with a high cholesterol diet. The results confirm that Anti-IL-6-USPIO have excellent IL-6-targeting ability and usefulness in detecting vulnerable plaques *in vitro* and *in vivo*, which may provide a novel, non-invasive strategy for evaluating acute cardiovascular risk or exploiting anti-atherosclerotic drugs.

Introduction

Atherosclerosis (AS) is a chronic inflammatory disease involved in the arterial system. Vulnerable plaque, a severe pathological characteristic form of plaques, is an essential factor that results in acute cardiovascular and cerebrovascular diseases.[1–3] Lots of clinical studies revealed that culprit lesions triggering occlusive coronary arterial thrombosis and myocardial infarction not infrequently have ≥50% lumen narrowing, which indicated that a considerable proportion of adverse events from coronary heart disease (CHD) affect patients without high-grade coronary artery stenosis.[4,5] Additionally, asymptomatic nonobstructive CHD has more difficulty in being discovered, leading to severe myocardial ischemia or infarction due to the development and rupture afterward of the mildly stenotic plaques.[6–8] Practical evaluation and prediction in the early process of plaques progression and vulnerability are of critical significance in the prevention of acute coronary syndrome and myocardial infarction. Currently, clinical invasive imaging techniques for atherosclerotic plaques mainly include coronary angiography (CAG), intravascular ultrasound (IVUS), and optical coherence tomography (OCT).[9,10] However, these imaging methods may result in the difficulty of obtaining information on early or developing vulnerable plaques in asymptomatic patients due to the limitation of invasive imaging techniques. Magnetic nanoparticles have a potential value in the early non-invasive detection of vulnerable plaques by magnetic resonance imaging without ionizing radiation.[11–14] Ultrasmall superparamagnetic iron oxide (USPIO) with a smaller diameter can reduce the clearance rate of the reticuloendothelial system (RES), increase the blood circulation time and enhance the phagocytosis of macrophages in plaque, which is useful for improving the MR imaging effect, but it can't reflect the characteristics of vulnerable plaques accurately.[15,16] Up to now, it still has some challenges to effectively evaluate and predict the stability and inflammatory activity of atherosclerotic plaques.[17,18]

The major pathological features of vulnerable plaques involve in macrophage infiltration, local inflammatory reaction, large lipid cores, and thin fibrous caps.[19–22] Foamy macrophages are the critical inflammatory cells involved in local inflammation and produce matrix metalloproteinases (MMPs) to degrade fibrin in the caps, which are strictly related to the vulnerability of atherosclerotic plaques.[23–26] Foamy macrophages can secrete a large number of inflammatory cytokines, including interleukin 1 (IL-1), IL-6, tumor necrosis factor (TNF-α), *etc.*[27–29] IL-6 is a specific inflammatory cytokine that plays a vital role in the development and rupture of atherosclerotic plaques. Studies have shown that IL-6 can be used as an independent marker for predicting future cardiovascular events.[30,31] A study shows that serum IL-6 levels in patients with carotid artery stenosis are

[a]*Department of Cardiology, Zhujiang Hospital, Southern Medical University, Guangzhou 510280, People's Republic of China. E-mail: ligxin@163.com*

[b]*Laboratory of Heart Center, Zhujiang Hospital, Sino-Japanese Cooperation Platform for Translational Research in Heart Failure, Guangdong Provincial Biomedical Engineering Technology Research Center for Cardiovascular Diseases, Guangzhou 510280, People's Republic of China. E-mail: skyer1@smu.edu.cn*

[c]*Department of Radiology, Zhujiang Hospital, Southern Medical University, Guangzhou 510280, People's Republic of China*

† Electronic supplementary information (ESI) available. See DOI: 10.1039/c9ra10509c

‡ These authors equally contributed to this work.

significantly higher than those in healthy people.[32] Koutouzis *et al.* confirm that serum IL-6 levels in patients with symptomatic carotid stenosis are considerably higher than those in patients with asymptomatic carotid stenosis, suggesting that inflammation may exacerbate the progression of stable asymptomatic plaques to unstable symptomatic plaques.[33] Therefore, IL-6 can potentially be an appropriate target for improving the MR imaging of macrophages and evaluating the inflammation and vulnerability of plaques.

In this study, IL-6 was used as a target to construct Anti-IL-6-USPIO. The characteristics of Anti-IL-6-USPIO in physics and biology were analyzed. By constructing IL-6-overexpressed macrophage model and rabbit abdominal aorta atherosclerosis model, we confirmed the IL-6-targeted feature of Anti-IL-6-USPIO and the usefulness as an MRI contrast agent for detection of vulnerable atherosclerotic plaques *in vitro* and *in vivo* experiments.

Materials and methods

Materials

Polyethylene glycol (PEG) coated ferrous oxide magnetic nanoparticles (USPIO) with carboxyl groups on the surface, provided by Dongna Biotech. Co. (Nanjing, China). 1-Ethyl-(3-dimethylaminopropyl) carbodiimide hydrochloride (EDC) and sulfo-*N*-hydroxysuccinimide (NHS) were purchased from Aladdin (Shanghai, China). Mouse anti-rabbit IL-6 monoclonal antibody and a nonspecific IgG antibody were purchased from Biosynthesis Biotech. Co. (Beijing, China). Borate-buffered saline (BBS) and phosphate-buffered saline (PBS) were obtained from Leagene Biotech. Co. (Beijing, China). Dulbecco's Modified Eagle Medium (DMEM) and fetal bovine serum (FBS) were obtained from Gibco Co. (Carlsbad, USA). Lipopolysaccharide (LPS) was acquired from Sigma Co. (St Louis, USA). RAW264.7 cells and human umbilical vein endothelial cells (HUVEC) were purchased from the Cell Bank of the Chinese Academy of Sciences (Shanghai, China).

Preparation of USPIOs

To prepare the Anti-IL-6-USPIO, 1 mg of PEG-coated USPIO (1 mg mL^{-1}) was diluted in ultrapure deionized water, and the pH value was adjusted to 5–6. 1 mg EDC and 0.5 mg sulfo-NHS were continuously added and stirred well in the shaking bed with 180 rpm at 25 °C for 25 min. After activation, 30 kD ultrafiltration tube was used to remove EDC/NHS, centrifuged two times with 4000 rpm for 30 min. The IL-6 monoclonal antibody solution was replaced by BBS (pH 8.5, 0.02 M) by 30 kD ultrafiltration tube to be centrifuged three times with 4000 rpm for 40 min. Then the antibodies solution was added in the activated USPIO and stirred for 2 h at room temperature. After the reaction, the Anti-IL-6-USPIO was purified by using magnetic separation column. The purified Anti-IL-6-USPIO was stored in PBS at 4 °C, which of concentration was 1 mg Fe per mL. IgG-USPIO was obtained by the same way. The morphology of the USPIO was characterized by transmission electron microscopy (TEM), the hydrodynamic dimension and zeta potential were measured by dynamic light scattering (DLS) and zeta potential analysis, and the immunological activity of molecular probes was detected by ELISA enzyme-linked immunosorbent assay.

Radioiodination of Anti-IL-6-USPIO

The chloramine-T method was used to label Anti-IL-6-USPIO. A mixture of 0.3 mL Anti-IL-6-USPIO (1 mg mL^{-1}), 1.5 mCi $Na^{125}I$ and 200 μL of chloramine-T in PBS (pH = 7.4, 4 mg mL^{-1}) in a polypropylene vial was shaken for 5 min, then 200 μL of $Na_2S_2O_5$ in PBS (pH = 7.4, 5 mg mL^{-1}) added vial to quench the iodination. The iodinated Anti-IL-6-USPIO was separated from excess reactants by passage through the centrifugation filtration and washed with water until the filtration solution was no gamma activity detectable. ^{125}I-Anti-IL-6-USPIO was dispersed in the saline solution.

Cell culture

The HUVEC cell line and macrophage cell line RAW264.7 cells were cultured with DMEM medium containing 10% fetal bovine serum (FBS) and 1% penicillin–streptomycin, cells were incubated in a saturating humidity atmosphere with 5% CO_2 at 37 °C.

Cytotoxicity assay for Anti-IL-6-USPIO

CCK-8 assay was used to evaluate the cytotoxicity of Anti-IL-6-USPIO. HUVEC was plated in 96-well plates (1×10^4 cells per well). Anti-IL-6-USPIO with different concentrations (0, 10, 20, 30, 40, 50 μg_{Fe} mL^{-1}) were incubated with these cells for 24 h and 48 h at 37 °C with 5% CO_2. Cell viability was evaluated by calculating the ratio of OD_{450} in the cells treated with Anti-IL-6-USPIO to OD_{450} in control cells without treatment.

Cell uptake of USPIOs

The uptake of various USPIOs by macrophage was evaluated by the Prussian blue staining. To perform the uptake experiments, 1×10^5 RAW264.7 macrophages were preincubated with DMEM containing 10% FBS with LPS (1 μg mL^{-1}) or without LPS for 24 h in 3.5 cm culture dish at 37 °C with 5% CO_2. Studies reported that RAW264.7 macrophages can be stimulated to overexpress IL-6 by LPS,[34,35] which immunofluorescence staining was performed for verification. RAW264.7 cells cultured with or without LPS were fixed in 4% paraformaldehyde and permeabilized with 0.5% Triton X-100 for 20 min. After being blocked with goat serum for 30 min at room temperature, cells were incubated with the primary antibody of Anti-IL-6 at 4 °C overnight. Then cells were incubated with Cy3-labeled Goat Anti-Rabbit IgG for 2 h at room temperature. Before being observed with a fluorescent microscope, cells were counterstained with DAPI. Cells under the same conditions above were incubated with various USPIOs (30 μg mL^{-1}) for an additional 12 h, including Anti-IL-6-USPIO, IgG-USPIO, and non-conjugated USPIO (NC-USPIO). In the competitive inhibition group, RAW264.7 cells were treated with 5 μg mL^{-1} of IL-6 monoclonal antibodies for 2 h before the administration of

Anti-IL-6-USPIO. The expression of IL-6 in RAW264.7 cells was determined by immunofluorescence. Intracellular iron oxide particles were identified by Prussian blue staining for evaluating the macrophage uptake of various USPIOs.

In vitro MR imaging

The Anti-IL-6-USPIO and NC-USPIO were mixed with 1% agarose gel in 50 mL EP tube respectively for different concentration (6, 12, 24, 30, 36 μg mL^{-1}). Different Gd-DTPA (16.8, 33.7, 67.3, 84.1, 100.9 μg mL^{-1}) also was mixed with 1% agarose gel respectively. 1×10^5 macrophages were incubated with various USPIOs and Gd-DTPA (Schering, Germany) for 12 h, washed with PBS for 3 times and fixed with 4% paraformaldehyde, then 1% agarose gel was respectively administered to Anti-IL-6-USPIO group, IgG-USPIO group, competitive inhibition group, NC-USPIO group, Gd-DTPA group, and water group. The enhanced MR images of materials with various concentration and different groups in cells were obtained by using a 7.0 T MR imaging scanner (Bruker, USA) equipped with suitable coils. The sequence and parameters of MRI were as follows, T_2 Turbo-RARE weighted sequence, TR = 2500 ms, TE = 35 ms, slice thickness = 0.7, matrix = 256 × 256. T_2 relaxation time and T_2 signal intensity ratio (rSI) were calculated. rSI = intracellular average signal intensity (SI_{cells})/ambient air average signal intensity (SI_{air}). The transverse relaxivity (r_2) equals the ratio of R_2 ($1/T_2$, s^{-1}) to Fe concentration of Anti-IL-6-USPIO.

Establishment of animal model

The animal experiments were conducted by using male New Zealand white rabbits, in which all animal procedures were performed in accordance with the Guidelines for the Care and Use of Laboratory Animals formulated by the Ministry of Science and Technology of China, and were approved by the Ethics Committee of the Southern Medical University. Nine rabbits weighing average 2.0 kg were purchased from Guangdong Medical Laboratory Animal Center. They were randomly divided into the experimental group (6 cases) and the control group (3 cases). Rabbits of the experimental group were damaged abdominal aortic intima with Foley's tube in combination with a high-fat diet (2% cholesterol, 4% lard, 94% basal diet) for 12 weeks to establish a model of atherosclerosis. The control group was fed with ordinary basal diet without special treatment for 12 weeks.

In vivo MR imaging

All animals were examined by Philips Intera Achieva 3.0 T magnetic resonance scanner (Philips, Netherlands). After anesthetized by 20% urethane solution, the animals were kept in supine position with phase resonance spinal coil. After obtaining the accurate position of abdominal aorta and right renal artery by performing 3D-TOF MRA, the right renal artery level was taken as the midpoint, and the range of scan was about 12 centimeters. The VISTA sequences of T_2WI and T_1WI were performed before and after enhancement. 40 layers of images were obtained by transversal scan. The sequence and parameters of MRI were as follows: (1) 3D-TOF MRA: TR 25 ms, TE 3 ms, FOV 130 mm × 130 mm, flip angle 20°, section thickness 1.3 mm, matrix 152 × 102, ETL 1. (2) T_1WI VISTA: TR 400 ms, TE 18 ms, FOV 120 mm × 120 mm, flip angle 90°, section thickness 3.0 mm, ETL 20, matrix 120 × 120, ETL 20. (3) T_2WI VISTA: TR 1500 ms, TE 264 ms, FOV 120 mm × 120 mm, flip angle 90°, section thickness 3.0 mm, matrix 120 × 120, ETL 80. After MR plain scan, all animals were immediately injected with Gd-DTPA 0.5 mmol kg^{-1} into the ear vein and scanned twice within 0.5 h. It is reported that gadolinium is less than 0.5 h in plasma half-life, and cleared from plasma within 24 h.[36] Third days, NC-USPIO (0.7 mg kg^{-1}) was injected through the marginal vein of ear, and MR was scanned at 24 h and 48 h after injection. Studies have shown that the negative reinforcement of USPIO enhanced MRI reaches its peak at 96 h, and then the T_2WI signal picks up.[37] On the 10th day, the MR images were obtained 24 h and 48 h after intravenous injection of Anti-IL-6-USPIO (0.7 mg kg^{-1}). MR image analysis was made by using Philips medical systems. According to the different time points before and after injection, the MR image group with same location was matched. The signal changes of the abdominal aortic plaque before and after intravenous infusion of NC-USPIO and Anti-IL-6-USPIO were compared according to MR images matched. The region of interest (ROI) was drawn on T_2 image sequence, and the mean signal intensity of the same abdominal aortic wall layer and the muscle signal intensity of the same layer were measured before and after MR enhancement. Signal intensities were measured by drawing four ROI at an equal distance of the same level. A signal-to-noise ratio (SNR) was calculated as follows:

$$\mathrm{SNR} = \frac{\text{mean value of abdominal aortic wall signal (SI)}}{\text{standard deviation of the muscle signal (SD)}}$$

The changes in SNR at different time points were observed at the same level. The images with more signal changes were selected after enhancement of Anti-IL-6-USPIO and NC-USPIO. 45 images from the experimental group and 15 images from the control group were selected to calculate the SNR and then compared, and 180 images were obtained according to different time points.

Histological analysis

After all MR scanning, all rabbits were anesthetized by an overdose of urethane and perfused with 100–200 mL PBS through the left ventricle. Aorta tissues were excised and fixed in 4% paraformaldehyde, then embedded in paraffin, sectioned and preserved at 4 °C. Pathological specimens were matched with MR images. HE staining, Masson staining, Prussian blue staining and immunohistochemistry (IL-6/CD68) were performed and observed under light microscope.

In vivo toxicity and biodistribution

500 microliters of blood were collected before the administration of nanoparticles (as control group) and 48 h after the administration of Anti-IL-6-USPIO for blood analysis. Blood indexes, including liver function (ALT, AST), kidney function

(BUN and CREA) and other blood indexes were analyzed to assess the toxicity of USPIO *in vivo*. ^{125}I labelled Anti-IL-6-USPIO was employed for examining the biodistribution of Fe-based nanoparticles *in vivo*. Firstly, animals were intravenously injected with ^{125}I-Anti-IL-6-USPIO (0.7 mg kg^{-1} of body weight, 30 μCi). At different time points after injection (1 h, 12 h, 24 h, 48 h), the blood and tissues from liver, kidney, heart, lung, stomach, spleen, muscle, bone of animals were collected, and the radioactivity in each tissue was countered by a gamma counter. Samples were weighted, the results were expressed in term of %ID/g = organ (tissue) count/injection count/weight of organ (tissue) × 100%.

Statistical analysis

All statistical analyses were carried out using SPSS 20.0. Data are presented as mean ± standard deviation. Comparison between two groups was made by *t*-test. The plaque detection rates between two contrast agents were compared by the chi-square test. When the theoretical frequency was less than 5 or the sample size was less than 40, the Fisher exact probability method was used. A value of $P < 0.05$ was considered statistically significant.

Results and discussion

Characteristic of USPIOs

The schematic of the preparation of the IL-6-targeted USPIO is shown in Scheme 1. PEG-2000 was coated with the iron oxide magnetic nanoparticles to endow them with carboxyl groups, and then the carboxyl groups were activated by sulfo-NHS.[38] The USPIO with PEGylation can reduce the non-specific recognization and clearance of the mononuclear phagocytic system (MPS) and prolong its blood circulation time.[15,39,40] The targeted USPIO was obtained by the conjugation of nanoparticles and IL-6 antibodies. TEM images (Fig. 1A and B) show that both NC-USPIO (without IL-6 conjugation) and Anti-IL-6-USPIO have a uniform spherical morphology in PBS solution. The mean sizes of two nanoparticles are 8.13 ± 0.75 nm and 12.3 ± 0.97 nm respectively (Fig. S1†). Although the NC-USPIO have the same iron core size, the hydrodynamic diameter distribution and zeta potential results show that the Anti-IL-6-USPIO have larger diameters and lower zeta potential than non-conjugated nanoparticles (82.98 ± 23.96 nm *vs.* 26.49 ± 7.91 nm, Fig. S1,† −22.6 mV *vs.* −34.6 mV, Fig. S2†),

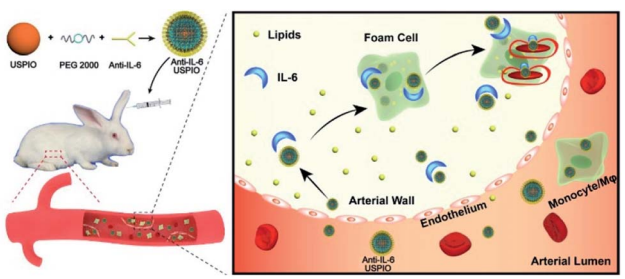

Scheme 1 Schematic illustration of Anti-IL-6-USPIO for targeted MR imaging of atherosclerotic vulnerable plaques in rabbits.

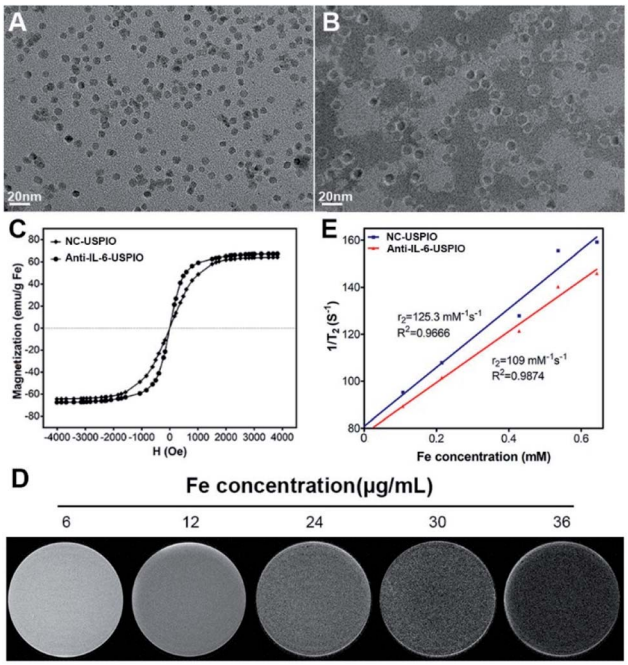

Fig. 1 TEM images of NC-USPIO (A) and Anti-IL-6-USPIO (B), saturation magnetization curve (C) of NC-USPIO and Anti-IL-6-USPIO, T_2 MR images of Anti-IL-6-USPIO with different concentrations (D), and the correlation between different concentrations and 1/T_2 in Anti-IL-6-USPIO and NC-USPIO (E).

which indicated the successful conjugation between the nanoparticles and the IL-6 antibody. The magnetization curves in Fig. 1C demonstrate that the non-conjugated and Anti-IL-6-USPIO are superparamagnetic with saturation magnetization values up to 64.34 and 67.29 emu g^{-1} at room temperature respectively. The relaxation signals of proton spin in the human body which excited by radiofrequency waves under a strong magnetic field is the key factor in MRI work,[41,42] and the iron oxide magnetic nanoparticles could reduce the transverse relaxation time T_2 effectively and then generate negative enhancement effects on T_2-related images.[43–46] The *in vitro* MRI result displays that Anti-IL-6-USPIO exhibit darker images with the increasing concentration of Fe, which indicates that the correlation between T_2 contrast enhancement effect and Fe (Fig. 1D). The transverse relaxivity (r_2) values of non-conjugated and Anti-IL-6-USPIO are calculated to be 125.3 mM^{-1} s^{-1} and 109.0 mM^{-1} s^{-1}, respectively (Fig. 1E). They are much larger than the r_2 value of Gd-DTPA (4.42 mM^{-1} s^{-1}) which mostly used for T_1-related imaging (Fig. S3†), and the slight gap of the r_2 benefits between NC-USPIO and Anti-IL-6-USPIO means that the conjugation of IL-6 antibody rarely influences the imaging effects of USPIO. ELISA results show that the Anti-IL-6 conjugated with USPIO retains relatively high biological activity, whereas the non-conjugated USPIO has inappreciable activity (Fig. S4†).

Cytotoxicity evaluation of USPIO

The cytotoxicity of Anti-IL-6-USPIO with HUVECs was evaluated by CCK-8 assays. As shown in Fig. S5,† the viability of HUVECs is 99%, 103%, 105% and 101% when the cells exposed to 10 μg mL^{-1}, 20 μg mL^{-1}, 30 μg mL^{-1} and 40 μg mL^{-1} of Anti-IL-6-

USPIO for a 48 h incubation. However, when the concentration of Anti-IL-6-USPIO rose to 50 μg mL^{-1}, the cell viability slightly decreases to 78%. These results imply that there is a favorable biocompatibility of Anti-IL-6 USPIO at the level ≤40 μg mL^{-1}.

Cellular uptake and *in vitro* MRI study

To verify the targeting effect of Anti-IL-6-USPIO on IL-6, we evaluate the cellular uptake of Anti-IL-6-USPIO by macrophages. Lipopolysaccharide (LPS) was used to stimulate a macrophage cell line of RAW264.7 cells for the LPS-induced secretion of IL-6. As shown in Fig. S6,† immunofluorescence staining experiments demonstrate that the expression of IL-6 was significantly increased in RAW264.7 with LPS induction compared with untreated cells. We also employ Fe staining assay to assess the cellular uptake of different USPIOs by RAW264.7 under two conditions (with or without LPS pre-treated), and the nonspecific IgG antibody is used to conjugate with USPIO to obtain the IgG-USPIO for the control group. Prussian blue staining results show that the cellular uptake of Anti-IL-6-USPIO by LPS pre-treated RAW264.7 is remarkably higher than IgG-USPIO and NC-USPIO. Moreover, the staining signals are almost suppressed when adding the blocking agent of 5 μg mL^{-1} Anti-IL-6 monoclonal antibody before the introduction of Anti-IL-6-USPIO for 2 h. On the other hand, the RAW264.7 without LPS pre-treated exhibits negligible binding affinity to different groups of USPIO (Fig. 2A). These results demonstrate the Anti-IL-6-USPIO has the capacity to target macrophages of over-expressed IL-6 excellently.

In vitro MRI study

Moreover, the *in vitro* T_2-weighted MRI effects of different USPIO groups in macrophages are evaluated. In light of the increased cellular uptake of Anti-IL-6-USPIO by LPS-induced RAW264.7, the activated macrophages incubated with Anti-IL-6-USPIO display stronger T_2 contrast enhancement effect than the groups incubated with other types of USPIO, which exhibit the darkest MR image (Fig. 2B). The relative signal intensity (rSI) results in Fig. 2C show that the difference is significant when other groups compared with the Anti-IL-6-USPIO group. Concretely, the rSI value of Anti-IL-6-USPO (3.77 9 ± 0.196) is nearly a quarter about that of NC-USPIO (15.744 ± 0.202). The rSI value of NC-USPIO is slightly more than the one in competitive inhibition group (13.290 ± 0.272), whereas is slightly less than the one of IgG-USPIO (18.296 ± 0.462). Compared to all of them, the water group (27.258 ± 0.492) has strongest rSI value, but the rSI value of Gd-DTPA (21.270 ± 0.266) declines more than that of water. These results indicate that Anti-IL-6-USPIO can decrease the rSI value of macrophages with over-expressed IL-6 significantly *in vitro* because of its IL-6 targeted characteristic.

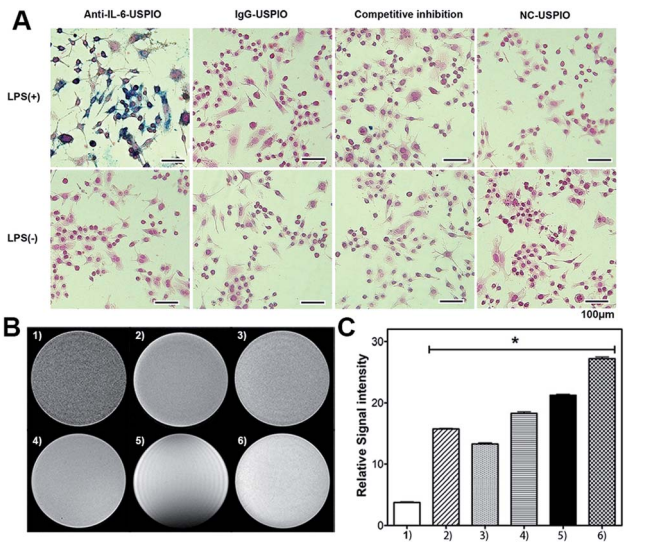

Fig. 2 Prussian blue staining of macrophages incubated with LPS or without LPS for 24 h before various USPIOs were added (A), T_2 MR images of induced macrophages incubated with various USPIOs for 12 h (B) and comparison of their rSIs (C), (1) to (6) are respectively Anti-IL-6-USPIO, NC-USPIO, competitive inhibiton, IgG-USPIO, Gd-DTPA and water, *P < 0.05 compared with Anti-IL-6-USPIO.

In vivo MRI study

Next, balloon injury surgery combines with a high-fat diet was implemented in New Zealand male rabbits for constructing an abdominal aortic atherosclerosis model. The success of the atherosclerosis model was confirmed by HE staining (Fig. S7†) and Masson staining (Fig. S8†). As shown in the two figures, atherosclerotic plaque shows lipid nucleus, foamy macrophages, thin fibrous cap (red arrows) or thick fibrous cap (blue arrows). The vulnerable plaque is characterized by large lipid nucleus, more foamy macrophages and thin fibrous cap. On the contrary, the staining images in the control group show smooth wall without thickening, intact endothelium, no lipid deposition under the endothelium, and smooth muscle cells in the media being slender, spindle-shaped and arranged neatly (black arrows). Afterward, we performed an MRI of the atherosclerotic lesions to confirm the IL-6-targeted characteristic of Anti-IL-6-USPIO and its capability to enhance the signal of T_2WI on plaque site. Fig. 3 shows representative images of the abdominal-aorta lesions at three-time points (pre, 24 h, and 48 h) following the administration of Anti-IL-6-USPIO with a dose of 0.7 mg kg^{-1} into the ear vein of rabbits. The significant signal loss is observed in the aortic wall at 24 h compared to pre-administration, and the negative enhancement effect of Anti-IL-6-USPIO could be extended to 48 h post the injection (Fig. 3C). The HE staining result of the scanning location of Fig. 3A–C is shown in Fig. 3D, which clearly indicates that the T_2 weighted imaging area is exactly the corresponding plaque position. Prussian blue and immunohistochemical staining were performed on the same layer of plaques and shown in Fig. S9.† The deposition of iron is confirmed by Prussian blue staining, and the staining results further show that there is a strong correlation between IL-6/macrophages ($CD68^+$)/positive Prussian blue staining, demonstrating the targeting ability of Anti-IL-6-USPIO in IL-6-enriched macrophages/foam cells.

We selected different contrast agents containing Anti-IL-6-USPIO, NC-USPIO, and Gd-DTPA to perform MR imaging of atherosclerotic lesions for further comparative analysis. As shown

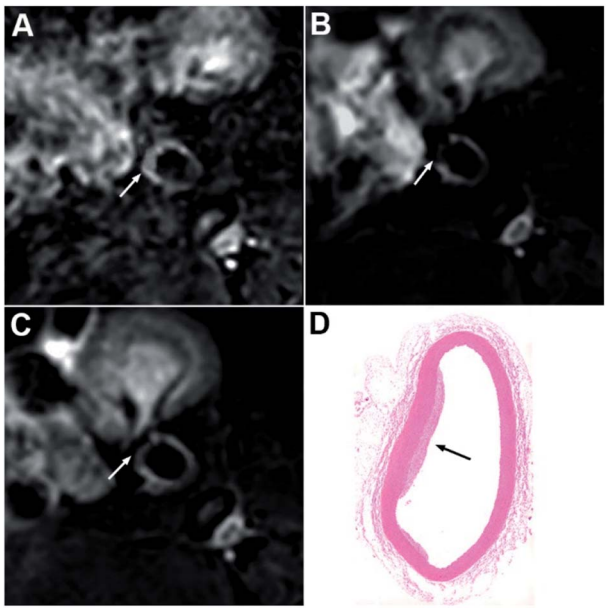

Fig. 3 T_2-weighted images at pre (A), 24 h (B) and 48 h (C) post injection of Anti-IL-6-USPIO. HE staining (D) shows the pathological section of the layer with plaque.

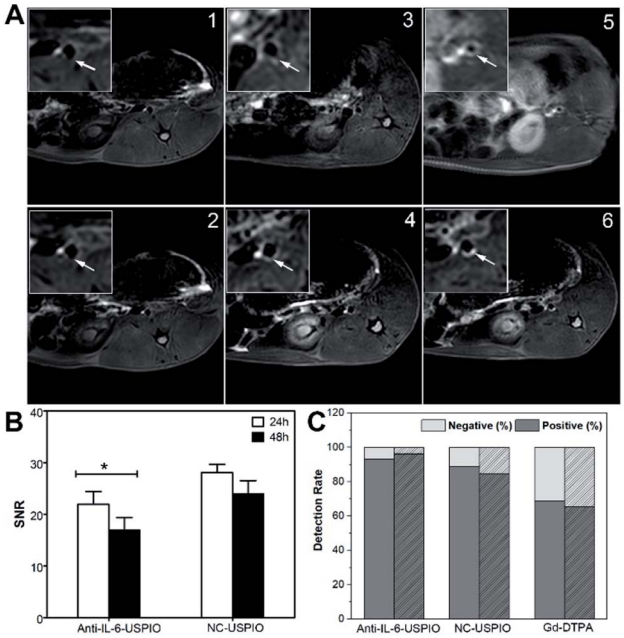

Fig. 4 T_2-weighted images after administration of Anti-IL-6-USPIO and NC-USPIO for 24 h (A1 and A3) and 48 h (A2 and A4) respectively, T_1-weighted images after Gd-DTPA enhancement scan (A5) and T_2-weighted images after plain scan (A6). Comparison of SNR in abdominal aortic walls 24 h and 48 h after injection of Anti-IL-6-USPIO and NC-USPIO in experimental group (B), $*P < 0.01$ *vs.* NC-USPIO group. Comparison of atherosclerotic and vulnerable plaques detection rate in three contrast agents respectively shows in left and right bars (C).

in Fig. 4A, compared with plain scanning, the T_2 signal of the plaque area after the administration of Anti-IL-6-USPIO and NC-USPIO for 24 h and 48 h both decrease significantly. The T_2 signal of the Anti-IL-6-USPIO group possesses a bigger decline than that of the NC-USPIO group, suggesting that Anti-IL-6-USPIO is more sensitive to T_2 signal changes of the plaque owing to its targeting, which contributes to a better imaging effect. The T_1 signal of the lesion post-injected Gd-DTPA is generally higher than that of the plain scanning, but the unstable T_1 signal of Gd-DTPA means that its detected efficiency on the plaques is not as good as the USPIOs. The ROI was calibrated on the T_2 images of the Anti-IL-6-USPIO group and the NC-USPIO group (24 h and 48 h), then the SNR values were calculated by the formula to obtain the results. The SNR values of Anti-IL-6-USPIO at 24 h and 48 h after injection are 21.94 ± 2.47 and 16.88 ± 2.47, whereas these values of NC-USPIO are 28.09 ± 1.58 and 23.98 ± 2.53, respectively, indicating the SNR of Anti-IL-6-USPIO in atherosclerotic plaques decrease significantly compared with that of NC-USPIO (Fig. 4B, Tables S1 and S2,† $P < 0.05$). The 45 images selected from the different groups were compared with the pathological sections, and the plaque detection rates of the three contrast agents were fully compared. As shown in Fig. 4C and Table S3,† the detection rates of atherosclerotic plaques are 93.3% (Anti-IL-6-USPIO), 88.9% (NC-USPIO), and 68.9% (Gd-DTPA). Among 45 pathological sections, 26 vulnerable plaques were confirmed, while the vulnerable plaques detected by Anti-IL-6-USPIO, NC-USPIO and Gd-DTPA are 25, 22 and 17, which the detection rates of vulnerable plaques are 96.2%, 84.6% and 65.4%, respectively (Fig. 4C and Table S4†). Comparing the detection rates of vulnerable plaques in three contrast agents, Anti-IL-6-USPIO has the highest detected accuracy.

In vivo toxicity and biodistribution

Afterward, the *in vivo* toxicity of Anti-IL-6-USPIO was investigated. The blood samples were collected before and 48 h after i.v. of Anti-IL-6-USPIO for blood analysis. The blood index of AST and ALT represented liver function and the index of BUN and CREA represented kidney function all kept up the normal level (Fig. S10A†), indicating that no obvious toxicity of the nanoparticles to liver and kidney. There were no remarkable changes in the other blood index, further clearly demonstrated that Anti-IL-6-USPIO had quite low toxicity *in vivo*. The biodistribution of Anti-IL-6-USPIO was assessed by examining the amount of ^{125}I labeled Anti-IL-6-USPIO in the blood, major organs, and tissues at different times (1, 12, 24, 48 h). As shown in Fig. S10B,† ^{125}I-Anti-IL-6-USPIO exhibited the long blood circulation time ($t_{1/2} = 11.39$ h) with a single exponential fitting, which was in favor of active targeting and enhanced permeability and retention property in the arterial lesion.[14] The biodistribution of ^{125}I-Anti-IL-6-USPIO was quantitatively analyzed to give an insight on the clearance pathways. From 1 h to 48 h, the uptake of ^{125}I-Anti-IL-6-USPIO in liver and kidney were decreased from 7.38 ± 1.49 ID g^{-1} and 2.16 ± 0.21 ID g^{-1} to 1.30 ± 0.26 ID g^{-1} and 0.18 ± 0.09 ID g^{-1}, respectively. Their downswing was consistent with that in blood, suggesting that ^{125}I-Anti-IL-6-USPIO could be excreted mainly from hepatic route and urine system. The ^{125}I-Anti-IL-6-USPIO in other organs and tissues disappeared with the time, indicating that

they were distributed temporally in these organs and tissues and could be efficiently cleared out within 48 h (Fig. S10C†). As a result, the efficient renal and hepatic clearance of ^{125}I-Anti-IL-6-USPIO enabled the ^{125}I-Anti-IL-6-USPIO particularly stable in the physiological environment and not easy to residue *in vivo*.

Conclusion

In summary, we have demonstrated a specific, sensitive, and biocompatible method for the non-invasive MR imaging of targeting IL-6 within atherosclerotic plaques, which may be more helpful to characterize macrophage infiltration and the stability of the atherosclerotic plaques. Anti-IL-6-USPIO shows high stability and high biological activity, as well as low toxicity. *In vitro* and *in vivo* studies demonstrate the IL-6-targeted characteristic of Anti-IL-6-USPIO and the usefulness as a MR negative contrast agent for detection of vulnerable atherosclerotic plaques. This method may have the potential to provide a novel, non-invasive technology for evaluating acute cardiovascular risk or exploiting anti-atherosclerotic drugs.

Conflicts of interest

There are no conflicts of interest to declare.

Acknowledgements

This research is supported by the National Natural Science Foundation of China (31900952, 51973090), the Natural Science Foundation of Guangdong Province, China (2014A020212724, 2018A030313446, 2019A1515011706, 2020A1515010288), and Clinical Research Startup Program of Southern Medical University by High-level University Construction Funding of Guangdong Provincial Department of Education (LC2016YM008).

References

1 V. Fuster, P. R. Moreno, Z. A. Fayad, R. Corti and J. J. Badimon, *J. Am. Coll. Cardiol.*, 2005, **46**, 937–954.
2 L. G. Spagnoli, A. Mauriello, G. Sangiorgi, S. Fratoni, E. Bonanno, R. S. Schwartz, D. G. Piepgras, R. Pistolese, A. Ippoliti and D. R. Holmes, Jr., *Jama*, 2004, **292**, 1845–1852.
3 D. Calvet, E. Touze, O. Varenne, J. L. Sablayrolles, S. Weber and J. L. Mas, *Circulation*, 2010, **121**, 1623–1629.
4 A. Arbab-Zadeh and V. Fuster, *J. Am. Coll. Cardiol.*, 2016, **68**, 2467–2478.
5 T. M. Maddox, M. A. Stanislawski, G. K. Grunwald, S. M. Bradley, P. M. Ho, T. T. Tsai, M. R. Patel, A. Sandhu, J. Valle, D. J. Magid, B. Leon, D. L. Bhatt, S. D. Fihn and J. S. Rumsfeld, *Jama*, 2014, **312**, 1754–1763.
6 R. S. Blumenthal, D. M. Becker, L. R. Yanek, T. R. Aversano, T. F. Moy, B. G. Kral and L. C. Becker, *Circulation*, 2003, **107**, 702–707.
7 M. C. Honigberg, B. S. Lander, V. Baliyan, M. Jones-O'Connor, E. W. Healy, J. E. Scholtz, J. T. Nagurney, U. Hoffmann, B. B. Ghoshhajra and P. Natarajan, *JACC: Cardiovasc. Imaging*, 2020, **13**, 437–448.
8 A. Ahmadi, E. Argulian, J. Leipsic, D. E. Newby and J. Narula, *J. Am. Coll. Cardiol.*, 2019, **74**, 1608–1617.
9 J. Sanz and Z. A. Fayad, *Nature*, 2008, **451**, 953–957.
10 C. Celeng, R. A. Takx, M. Ferencik and P. Maurovich-Horvat, *Trends Cardiovasc. Med.*, 2016, **26**, 538–547.
11 L. P. Smits, F. Tiessens, K. H. Zheng, E. S. Stroes, A. J. Nederveen and B. F. Coolen, *Atherosclerosis*, 2017, **263**, 211–218.
12 Z. Zhou, J. Song, R. Tian, Z. Yang, G. Yu, L. Lin, G. Zhang, W. Fan, F. Zhang, G. Niu, L. Nie and X. Chen, *Angew. Chem., Int. Ed.*, 2017, **56**, 6492–6496.
13 G. Gitsioudis, Y. S. Chatzizisis, P. Wolf, A. Missiou, A. P. Antoniadis, D. Mitsouras, S. Bartling, Z. Arica, M. Stuber, F. J. Rybicki, M. Nunninger, C. Erbel, P. Libby, G. D. Giannoglou, H. A. Katus and G. Korosoglou, *Eur. Heart J. Cardiovasc. Imaging*, 2017, **18**, 19–30.
14 Y. Liu, X. Lv, H. Liu, Z. Zhou, J. Huang, S. Lei, S. Cai, Z. Chen, Y. Guo, Z. Chen, X. Zhou and L. Nie, *Nanoscale*, 2018, **10**, 3631–3638.
15 X. Zhao, H. Zhao, Z. Chen and M. Lan, *J. Nanosci. Nanotechnol.*, 2014, **14**, 210–220.
16 S. R. Alam, C. Stirrat, J. Richards, S. Mirsadraee, S. I. Semple, G. Tse, P. Henriksen and D. E. Newby, *J. Cardiovasc. Magn. Reson.*, 2015, **17**, 83.
17 J. M. S. Chan, C. Monaco, M. Wylezinska-Arridge, J. L. Tremoleda, J. E. Cole, M. Goddard, M. S. H. Cheung, K. K. Bhakoo and R. G. J. Gibbs, *J. Vasc. Surg.*, 2018, **67**, 1571–1583.
18 H. Qiao, Y. Wang, R. Zhang, Q. Gao, X. Liang, L. Gao, Z. Jiang, R. Qiao, D. Han, Y. Zhang, Y. Qiu, J. Tian, M. Gao and F. Cao, *Biomaterials*, 2017, **112**, 336–345.
19 C. Stefanadis, C. K. Antoniou, D. Tsiachris and P. Pietri, *J. Am. Heart Assoc.*, 2017, **6**, e005543.
20 A. P. Burke, A. Farb, G. T. Malcom, Y. Liang, J. E. Smialek and R. Virmani, *Jama*, 1999, **281**, 921–926.
21 A. Buffon, L. M. Biasucci, G. Liuzzo, G. D'Onofrio, F. Crea and A. Maseri, *N. Engl. J. Med.*, 2002, **347**, 5–12.
22 A. V. Finn, M. Nakano, J. Narula, F. D. Kolodgie and R. Virmani, *Arterioscler., Thromb., Vasc. Biol.*, 2010, **30**, 1282–1292.
23 G. K. Hansson, *N. Engl. J. Med.*, 2005, **352**, 1685–1695.
24 W. Peeters, F. L. Moll, A. Vink, P. J. van der Spek, D. P. de Kleijn, J. P. de Vries, J. H. Verheijen, A. C. Newby and G. Pasterkamp, *Eur. Heart J.*, 2011, **32**, 2314–2325.
25 J. L. Johnson, *Eur. J. Pharmacol.*, 2017, **816**, 93–106.
26 A. C. Newby, S. J. George, Y. Ismail, J. L. Johnson, G. B. Sala-Newby and A. C. Thomas, *Thromb. Haemostasis*, 2009, **101**, 1006–1011.
27 M. Nahrendorf, M. J. Pittet and F. K. Swirski, *Circulation*, 2010, **121**, 2437–2445.
28 D. A. Chistiakov, Y. V. Bobryshev and A. N. Orekhov, *J. Cell. Mol. Med.*, 2015, **19**, 1163–1173.
29 A. Ghattas, H. R. Griffiths, A. Devitt, G. Y. Lip and E. Shantsila, *J. Am. Coll. Cardiol.*, 2013, **62**, 1541–1551.

30 P. M. Ridker, N. Rifai, M. J. Stampfer and C. H. Hennekens, *Circulation*, 2000, **101**, 1767–1772.
31 E. Lindmark, E. Diderholm, L. Wallentin and A. Siegbahn, *Jama*, 2001, **286**, 2107–2113.
32 E. Debing, E. Peeters, C. Demanet, M. De Waele and P. Van den Brande, *Vasc. Endovasc. Surg.*, 2008, **42**, 122–127.
33 M. Koutouzis, L. S. Rallidis, G. Peros, A. Nomikos, V. Tzavara, C. Barbatis, V. Andrikopoulos, J. Vassiliou and Z. S. Kyriakides, *Acta Neurol. Scand.*, 2009, **119**, 119–125.
34 Y. H. Kim, J. R. Noh, J. H. Hwang, K. S. Kim, D. H. Choi, J. P. An, W. K. Oh and C. H. Lee, *Exp. Ther. Med.*, 2017, **14**, 5863–5870.
35 Y. Takahashi, R. Watanabe, Y. Sato, N. Ozawa, M. Kojima, K. Watanabe-Kominato, R. Shirai, K. Sato, T. Hirano and T. Watanabe, *Metabolism*, 2018, **83**, 128–138.
36 S. H. Kim, K. G. Csaky, N. S. Wang and R. J. Lutz, *Pharm. Res.*, 2008, **25**, 512–520.
37 T. Sha, C. Qi, W. Fu, J. I. Hao, L. Gong, H. Wu and Q. Zhang, *Exp. Ther. Med.*, 2016, **12**, 141–146.
38 J. Xie, C. Yan, Y. Yan, L. Chen, L. Song, F. Zang, Y. An, G. Teng, N. Gu and Y. Zhang, *Nanoscale*, 2016, **8**, 16902–16915.
39 A. Usman, U. Sadat, A. J. Patterson, T. Y. Tang, K. Varty, J. R. Boyle, M. P. Armon, P. D. Hayes, M. J. Graves and J. H. Gillard, *Nanomedicine*, 2015, **10**, 3077–3087.
40 L. Chen, F. Zang, H. Wu, J. Li, J. Xie, M. Ma, N. Gu and Y. Zhang, *Nanoscale*, 2018, **10**, 1788–1797.
41 G. Yue, A. L. Alexander, D. H. Laidlaw, A. F. Gmitro, E. C. Unger and R. M. Enoka, *J. Appl. Physiol.*, 1994, **77**, 84–92.
42 J. I. Hamilton, Y. Jiang, Y. Chen, D. Ma, W. C. Lo, M. Griswold and N. Seiberlich, *Magn. Reson. Med.*, 2017, **77**, 1446–1458.
43 Z. Zhou, L. Yang, J. Gao and X. Chen, *Adv. Mater.*, 2019, **31**, e1804567.
44 L. Yang, Z. Wang, L. Ma, A. Li, J. Xin, R. Wei, H. Lin, R. Wang, Z. Chen and J. Gao, *ACS Nano*, 2018, **12**, 4605–4614.
45 Z. Zhao, Z. Zhou, J. Bao, Z. Wang, J. Hu, X. Chi, K. Ni, R. Wang, X. Chen, Z. Chen and J. Gao, *Nat. Commun.*, 2013, **4**, 2266.
46 Z. Zhou, R. Tian, Z. Wang, Z. Yang, Y. Liu, G. Liu, R. Wang, J. Gao, J. Song, L. Nie and X. Chen, *Nat. Commun.*, 2017, **8**, 15468.